

Spreading droplets of yield-stress fluids with and without gravity

Linnea Heitmeier,^{1,2} Olfa D'Angelo,^{3,1} Maziyar Jalaal,⁴ and Thomas Voigtmann^{1,2}

¹*Institute for Frontier Materials on Earth and in Space, German Aerospace Center (DLR), 51170 Köln, Germany*

²*Department of Physics, Heinrich-Heine Universität Düsseldorf, Universitätsstraße 1, 40225 Düsseldorf, Germany*

³*Institut Supérieur de l'Aéronautique et de l'Espace (ISAE-SUPAERO), Université de Toulouse, Toulouse, France*

⁴*Van der Waals-Zeeman Institute, University of Amsterdam, Science Park 904, 1098 XH Amsterdam, The Netherlands*

(*Electronic mail: linnea.heitmeier@dlr.de)

(Dated: 8 July 2025)

We investigate the effect of gravity on the spreading of droplets of yield stress fluids, by performing both microgravity experiments (in a drop tower) and experiments under terrestrial gravity. We investigate the dependence of the final droplet shape on yield stress and gravity. Droplets are deposited on a thin film of the same material, allowing to directly test scaling laws derived from the thin-film equation for viscoplastic fluids. Microgravity conditions allow to vary independently the two relevant dimensionless numbers, the Bond number \mathcal{B} and the plastocapillary number \mathcal{J} , and thus to disentangle the influence of surface tension from that of the yield stress on the droplet shapes. Simulations using a visco-elastic model with shear thinning complement the experiments and show good agreement regarding the droplet shapes. Possible deviations arising in the regime of non-negligible elastic effects and large plastocapillary numbers (large yield stress) are discussed.

I. INTRODUCTION

Yield-stress fluids (YSFs) are characterized by their dual rheological response: they flow like (complex) fluids only when the applied stress exceeds a threshold (the yield stress). Below this threshold, their deformation behavior becomes solid-like [1, 2]. This invites a wide range of applications: many commonly used materials such as pastes, gels, emulsions, foams, and a variety of biological and industrial suspensions exhibit a yield stress [3]. As a result, the spreading of YSFs (and in general non-Newtonian fluids) is central to many processes in sectors including food processing, cosmetics, pharmaceuticals, construction, and energy. For example, the presence of a yield stress in 3D-printing materials ensures that extruded filaments or droplets retain their shape after deposition, enabling the controlled, layer-by-layer fabrication of complex structures [4–8].

Despite this practical importance, some fundamental aspects of the spreading of YSFs have only been established recently [9–12]. A defining characteristic of YSFs is that their droplets reach a finite size even on fully wetting substrates. Unlike Newtonian fluids, which would theoretically spread indefinitely into an infinitesimally thin film, YSFs balance hydrostatic pressure and surface tension against the yield stress, resulting in droplets of finite radius. This principle underpins direct-ink writing technologies, and notably bioprinting [13–15] both on ground and in space [16]. We are therefore interested in how the asymptotic droplet size – achieved at long times, $t \rightarrow \infty$ after extrusion – depends on parameters such as the deposited fluid volume, material properties, and gravity.

Since the formation and spreading of YSF droplets is mainly governed by three factors – yield stress, surface tension, and hydrostatic pressure – (at least) two dimensionless groups are needed to characterize their flow properties [11]. The Bond number, \mathcal{B} , quantifies the importance of gravity over surface tension, and is well known from the spreading of Newtonian fluids. The existence of a yield stress implies another relevant dimensionless quantity, the plastocapillary number, \mathcal{J} , to

quantify the importance of yield-stress effects over surface-tension ones. For a droplet of typical length-scale \mathcal{L} (to be defined more precisely further below) and fluid mass density ρ , one defines

$$\mathcal{B} = \frac{\rho g \mathcal{L}^2}{\hat{\sigma}}, \quad \mathcal{J} = \frac{\tau_0 \mathcal{L}}{\hat{\sigma}}. \quad (1)$$

Here, τ_0 is the yield stress, $\hat{\sigma}$ the surface tension, and g the gravitational acceleration. Specifically, scaling laws were derived for the standard viscoplastic Bingham model [11] that predict the asymptotic droplet radius R as a function of the dimensionless numbers. A particularly intriguing aspect of these laws is the emergence of distinct scaling exponents when $\mathcal{B} = 0$, highlighting this regime as one where further experimental studies are desired.

To vary the dimensionless numbers \mathcal{B} and \mathcal{J} , the length scale \mathcal{L} is arguably the parameter that is most easily changed in Eqs. (1). However, this does not allow to change both numbers independently. Especially realizing the limit $\mathcal{B} \rightarrow 0$ via $\mathcal{L} \rightarrow 0$, *i.e.* in infinitely small droplets, implies both $\mathcal{J} \rightarrow 0$ and obvious experimental limitations. To access a broader range of the parameter space and vary \mathcal{B} and \mathcal{J} independently, we opt to vary the effective gravitational acceleration, g . This allows us to probe the limit $\mathcal{B} \rightarrow 0$ while keeping \mathcal{J} finite.

The study of droplets in the regime $g \rightarrow 0$ has hitherto mostly focused on Newtonian fluids. Surface tension measurements on droplets under such effective microgravity conditions have a long-established history [17]. Sessile droplets have also been studied at $g \rightarrow 0$ to assess variations in contact angles and wettability [18–21]. The coalescence of sessile water drops has been studied on the International Space Station (ISS), investigating the contact line motion at small Bond numbers, while taking advantage of the enhanced optical resolution brought by large droplets [22, 23].

Non-Newtonian droplet studies in the limit $g \rightarrow 0$ have been proposed as a promising way to investigate fluid parameters, such as surface tension and viscosity, by means of levitation and droplet oscillations [24]. However, to date, nearly all

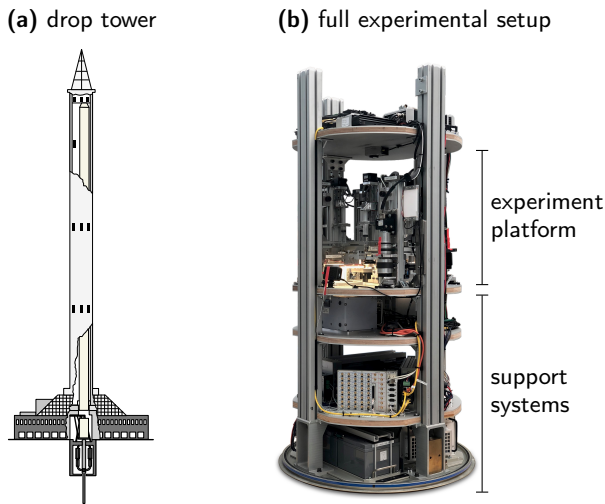


FIG. 1. Platform used to conduct microgravity experiments. (a) Schematic of the ZARM drop tower, including catapult system below. (b) Full experimental capsule, including experimental platform and support systems.

studies have been conducted under Earth gravity, primarily focusing on the spreading of sessile and impacting droplets [12, 25–28]. More applied studies include experimental setups mimicking inkjet printing [29] or Leidenfrost droplets [30].

We present results from microgravity experiments; by this, we denote experiments performed in a freely falling setup where gravitational acceleration effectively vanishes. In this regime, we test the scaling laws for the final droplet radius that were predicted by Jalaal, Stoeber, and Balmforth [11]. While previous experimental and simulation studies have explored these laws [8, 12], the ability to independently vary both \mathcal{B} and \mathcal{J} in our microgravity experiments enables a far more stringent test of the theoretical predictions. Our findings show agreement with the theoretical power laws, including their predicted asymptotic prefactors. Some systematic deviations appear that we discuss in the context of non-vanishing elastic effects. Complementary simulations show that a shear-thinning visco-elastic fluid is a good model system for the observed droplet shapes.

II. METHODS

A. Experiments

We conducted microgravity experiments ($g \rightarrow g_\mu \approx 0$) complemented by ground-based experiments (in nominal Earth gravitational acceleration, $g_E = 9.8 \text{ m s}^{-1}$). Experimental campaigns were performed at the Center of Applied Space Technology and Microgravity (ZARM) drop tower in Bremen, Germany [31–33] (see Fig. 1). Taking advantage of its catapult system, the ZARM drop tower provides a total of 9.3 s of microgravity ($g_\mu < 10^{-4} \text{ m s}^{-1}$). Ground reference experiments were conducted in the same setup, using the same sample batches as the corresponding microgravity experiment, and

label	composition	yield stress
c1	0.3 wt%	6.5 Pa
c2	0.35 wt%	9 Pa
c3	0.4 wt%	14 Pa
c4	0.45 wt%	21 Pa
c5	0.5 wt%	35 Pa
c6	0.55 wt%	55 Pa

TABLE I. Concentration and yield-stress values of the Carbopol aqueous solutions used in the experiments, with the labels used in the text and figure captions as reference.

usually on the same day, a few hours prior. A detailed description of the hardware is provided elsewhere [34]. Below, we summarize the main steps of the experimental procedure.

The experiment consists of the deposition of a droplet of complex fluid on a pre-wetted glass substrate covered by a thin film of the same fluid (see Fig. 2). The initial wetting of the substrate is done by rotating a rotary stage onto which the substrate is mounted, underneath a custom-designed nozzle-and-blade system. The latter is designed to cover the glass surface with a thin fluid film. Importantly, for the microgravity experiments, the thin film and droplet are both deposited during the microgravity phase [34]. Subsequently, a droplet is extruded through a nozzle placed in the center of the droplet (inner diameter 0.8 mm, placed at 0.8 mm above the substrate). The glass surfaces are chemically treated to avoid slip [35]. The droplet volume, V , is controlled by a linear motor driving the extrusion syringe. The volumes deposited are $V = 0.5 \text{ mL}$, 1.8 mL , 4.2 mL , and 5.6 mL . Different extrusion speeds were used, but found to have no influence on the asymptotic droplet shapes discussed here. For later reference, unless otherwise specified, we give the corresponding length scale \mathcal{L} as the diameter of a sphere with the same volume, *i.e.*, $\mathcal{L} = (6V/\pi)^{1/3}$. The corresponding values are $\mathcal{L} = 1.0 \text{ cm}$, 1.5 cm , 2.0 cm and 2.2 cm . (We omit the unit when quoting \mathcal{L} values where convenient in the following.)

Pre-wetting takes around 1.4 s, and we find that the droplets attain stationary final shapes well within the remaining microgravity time for these parameters. The video recordings from all experiments are available online [36].

The droplets' spread is measured using shadowgraphy, a straightforward method for extracting the temporal evolution of axisymmetric droplet shapes. For this, the droplet is illuminated from one side using a custom-made LED panel, and observed from the opposite side using a high-speed camera. The resulting images are subject to a standardized image-analysis technique described in Appendix A. We specifically extract the final droplet radius, R , and final height, h , from these images. For the radius, two values are extracted from the left- and right-hand part of the images, and both values are shown to indicate the precision of the measurement.

The complex fluids used as experimental materials are Carbopol aqueous solutions, widely studied as model viscoplastic fluids [2, 11, 37–42]. Six different concentrations (labels c1 to c6) were used, ranging from 0.3 wt% to 0.55 wt%, corresponding to yield stresses, τ_0 , between 6.5 Pa and 55 Pa (see

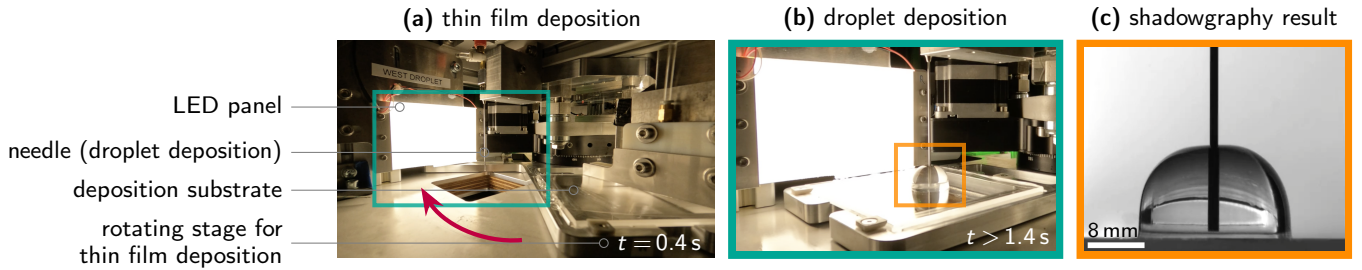


FIG. 2. Experimental setup and procedure for one droplet. (a) The thin film is deposited by rotating the substrate underneath a disposal blade (red arrow). (b) The droplet is deposited through a needle. (c) Exemplary shadowgraphy result.

Table I for the precise values). Experiments cover a large (but not complete) set of combinations of droplet sizes and concentrations. All solutions were produced by dilution from a 1 wt% stock solution. The latter was prepared by dispersing poly acrylic acid (PAA) powder (Sigma Aldrich) in Milli-Q water using a four-blade marine impeller rotating at 1000 rpm to 1500 rpm at room temperature, and thereafter neutralizing the solution to pH 7 with triethanolamine (Sigma Aldrich). The yield stress values of the solutions are obtained using an Anton Paar rheometer (MCR-502), measuring flow curves by increasing the shear rate from 0.01 s^{-1} to 1000 s^{-1} and fitting a Herschel-Bulkley model through the flow-curve data.

Note that from Eq. (1) one infers the droplet sizes for which gravitational effects become relevant. This is usually expressed through the capillary length $l_\kappa = \sqrt{\hat{\sigma}/\rho g}$, such that $\mathcal{B} = (\mathcal{L}/l_\kappa)^2 \gg 1$ if $\mathcal{L} \gg l_\kappa$. For a typical liquid density of $\rho \approx 1 \cdot 10^3 \text{ kg m}^{-3}$, and with a the surface tension of water, $\hat{\sigma} = 0.072 \text{ N m}$, as a reference, we obtain $l_\kappa \approx 2.7 \text{ mm}$. All our experimental data is in the regime $\mathcal{L} \gg l_\kappa$.

B. Simulations

The experiments are complemented by fluid dynamics simulations, carried out using the open-source tool BASILISK C, a C-like programming language adapted specifically to the task [43, 44].

In BASILISK, the volume of fluid technique is used to track the interface between the droplet fluid and a surrounding low-density, low-viscosity fluid (representing ambient air). A color function f is used (where $f = 1$ in the liquid and $f = 0$ in the gas), which satisfies the scalar-advection equation. One solves the governing equations using a one-fluid approximation [45, 46], using adaptive mesh refinement based on wavelet estimated discretization errors. The solver has been extensively used for various Newtonian and non-Newtonian problems with deformable interfaces [11, 12, 28, 47–49].

The governing equations are given by the mass-conservation equation for incompressible fluids, $\nabla \cdot \mathbf{v} = 0$, and the momentum conservation equation,

$$\rho \frac{D}{Dt} \mathbf{v} = -\nabla p + \nabla \cdot \boldsymbol{\sigma} + \mathbf{f}_{\text{ext}}, \quad (2)$$

where \mathbf{f}_{ext} is an external force density representing gravita-

tional force, if present. For the stress tensor, $\boldsymbol{\sigma}$, we use the constitutive equation of a shear-thinning viscoelastic fluid that is representative of a glass-forming fluid with a dynamical yield stress that emerges at the glass transition [50, 51].

Specifically, we set $\boldsymbol{\sigma} = \eta_N \dot{\boldsymbol{\gamma}} + \boldsymbol{\sigma}_p$, where η_N is a Newtonian background viscosity, and $\dot{\boldsymbol{\gamma}} = (\nabla \mathbf{v}) + (\nabla \mathbf{v})^T$ the symmetrized shear-rate tensor. The non-Newtonian contribution is modeled in a form known as a White-Metzner model from rheology,

$$\frac{1}{\tau(\|\dot{\boldsymbol{\gamma}}\|)} \boldsymbol{\sigma}_p + \overset{\nabla}{\boldsymbol{\sigma}}_p = G_\infty \dot{\boldsymbol{\gamma}}. \quad (3)$$

For fixed relaxation time $\tau = \tau_{\text{eq}}$, this is the standard upper-convected Maxwell model (Oldroyd-B model including the Newtonian background viscosity). The symbol $\overset{\nabla}{\boldsymbol{\sigma}}$ indicates the upper-convected time derivative, defined by

$$\overset{\nabla}{A} = \frac{d}{dt} A - (\nabla \mathbf{v})^T \cdot A - A \cdot (\nabla \mathbf{v}) \quad (4)$$

for a twice-contravariant tensor A such as the stress tensor [52].

The Oldroyd-B model describes viscoelastic stress relaxation: for time scales $t \ll \tau_{\text{eq}}$, the response is that of an elastic solid, while for $t \gg \tau_{\text{eq}}$, viscous flow sets in, with a non-Newtonian contribution to the viscosity $\eta_p = G_\infty \tau_{\text{eq}}$.

To include the effect of shear-thinning, we introduce a shear-rate dependent relaxation rate: we set

$$\tau^{-1} = \tau_{\text{eq}}^{-1} + \frac{\|\dot{\boldsymbol{\gamma}}\|}{\gamma_c} \quad (5)$$

in Eq. (3). This form is inspired by microscopic approaches to the rheology of glass-forming colloidal suspensions and has been referred to as a “nonlinear Maxwell model” [50, 51]. In the limit $\tau_{\text{eq}} \rightarrow \infty$, this model describes a YSF, with a yield stress $\tau_0 = G_\infty \gamma_c$. For finite τ_{eq} , the model describes a quasi-YSF, regularizing the infinite zero-shear viscosity by a finite one. For the numerical simulations considered here, we set $\tau_{\text{eq}} = 50 \text{ s}$, large enough to consider our simulations to be in the YSF regime. Asymptotic droplet shapes are measured in a time window where the initial relaxation of the fluid has passed, but on a time scale $t < \tau_{\text{eq}}$ before viscous relaxation sets in. (See below for specific examples.)

The simulations consider droplet spreading in cylindrical symmetry, assuming the z -axis to be the symmetry axis (and transforming the Navier-Stokes equations into the corresponding coordinate system). Cross-sections are thus obtained in

the (x, z) -axis, and gravity, if present, acts in the negative z -direction. The initial conditions are that of a rotation ellipsoid, given by

$$x^2 + (\zeta z)^2 = R_0^2, \quad (6)$$

with $\zeta = 3$ to allow for the relaxation of prolate droplets to flatter shapes. The conversion between experimental values \mathcal{L} and simulated radius R_0 is thus $\mathcal{L} = R_0 \cdot (4/\zeta)^{1/3}$. Further, a pre-wetted film of thickness $h_\infty = 1$ mm is added to the simulations for numerical stability.

As further simulation details, the fraction of densities is fixed as $\rho_{\text{air}}/\rho_{\text{fluid}} = 0.001$, and the fraction of Newtonian viscosities $\eta_{\text{air}}/\eta_{\text{fluid}} = 0.1$. A box of side length $L_x = 0.1$ m (large enough to prevent finite size effects), and a resolution level of 8 for adaptive mesh refinement in BASILISK were chosen for the simulations. The value of the surface tension $\hat{\sigma} = 0.07 \text{ N m}^{-1}$ mimics that of a typical non-surfactant aqueous suspension. For the constitutive equation, Eq. (3), $\gamma_c = 1/5$ is fixed; this sets a typical strain scale where plastic yielding starts to dominate over elastic response in the model, and values of that order are to be expected on the grounds of microscopic theory [50]. To adjust the yield stress, we vary the Maxwell shear modulus, $G_\infty = 32.5 \text{ Pa}, 45 \text{ Pa}, 70 \text{ Pa}, 105 \text{ Pa}, 175 \text{ Pa},$ and 275 Pa , such that the simulated fluids have the same yield stress values as determined for the Carbopol solutions used in the experiment. Note that in this model, elasticity and yield stress are linked; the addition of elastic effects is an extension of the simpler Bingham viscoplastic model used in the theory [11]. Our viscoelastic shear-thinning model is also distinct from elastoviscoplastic models that incorporate an ad-hoc yield stress and that have recently been used to study droplet spreading [12].

III. RESULTS

A. Droplet shapes

We begin by analyzing the droplet shapes obtained in the experiments. Figure 3 shows exemplary height functions obtained from the image analysis, for a fixed concentration (fluid c4, *cf.* Tab. I) and different droplet sizes, for microgravity [Fig. 3(a)] and Earth gravity [Fig. 3(b)] experiments. One can observe that the droplet shapes are clearly different depending on g . For the concentration and range of parameters shown in the figure, the droplets in microgravity are taller due to the lack of hydrostatic pressure, and therefore consequently less wide at the same volume than under Earth gravity.

All droplets considered here correspond to non-negligible Bond number. For $\mathcal{L} = 1$ cm (smallest droplet), we get $\mathcal{B} \approx 14$ in Earth gravity, or $\mathcal{B}_h = \mathcal{B}/4^{2/3} \approx 5.4$ if we calculate the Bond number from the expected height of the droplet. Comparing the droplet shapes in g_μ and g_E (Fig. 3(a) to (b)), we see that in this case, the droplet shapes are still little influenced by g . For larger \mathcal{L} , the gravity-induced flattening of the droplets becomes more and more apparent. The largest droplets in microgravity (Fig. 3(a)) are reasonably close to half-spheres, indicated by dashed lines. However, while this is true for this specific fluid, it does not generalize to other concentrations – we

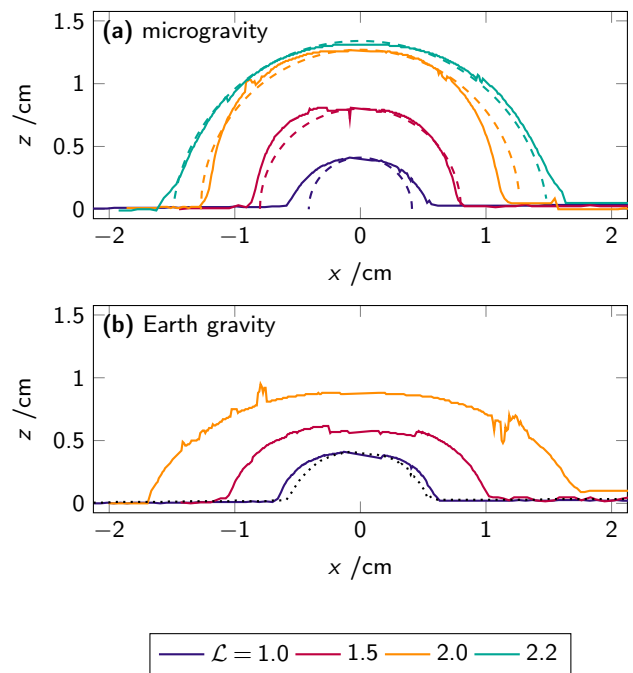


FIG. 3. Experimental droplet shapes for different volumes ($\mathcal{L} = 1$ cm, 1.5 cm, 2 cm and 2.2 cm from bottom to top) for concentration c4. Solid lines are reconstructed from image analysis, shown for (a) microgravity experiments and (b) experiments in Earth gravity. (Note that $\mathcal{L} = 2.2$ cm is missing in the latter.) In (a), dashed lines correspond to half-spheres as a comparison. In (b), a dotted line replicates the $\mathcal{L} = 1$ cm result from (a) to ease comparison.

return below to a discussion of the concentration-dependence of droplet shapes.

While the droplet volume is in principle fixed by the automated deposition system, we account for possible deviations in the finally extruded volume. To this end, the droplet cross-sections extracted from the image analysis are numerically integrated to obtain their volume. Assuming cylindrical symmetry around the z axis, we obtain $V_{\text{exp}} = 2\pi \int_{x \geq 0} x z(x) dx$. In the experiments, we confirmed by shadowgraphy also from below for some droplets their cylindrical symmetry (see Appendix A for details and images). The integral is taken over either positive x or negative x , resulting in two estimates for V_{exp} . Note that the image analysis tends to systematically underestimate $z(x)$: reflections from the light source sometimes cause bright features inside the shadowgraphy projection of the droplet. We thus obtain V_{exp} as the larger of the two integrals. This estimate of the extruded volume defines the experimentally corrected droplet length scale, $\mathcal{L}_{\text{eff}} = (6/\pi)V_{\text{exp}}$.

The resulting \mathcal{L}_{eff} are compared with the nominal \mathcal{L} in Fig. 4. We see that in particular in Earth gravity (open symbols), the reconstructed droplet volumes sometimes show large deviations from the expected ones, droplets often appearing smaller than expected. The microgravity data is much closer to the expected trend.

Discrepancies between \mathcal{L} and \mathcal{L}_{eff} arise from two main sources apart from poor reconstruction by image analysis. In the experiments, great care was taken to avoid air inclusions in

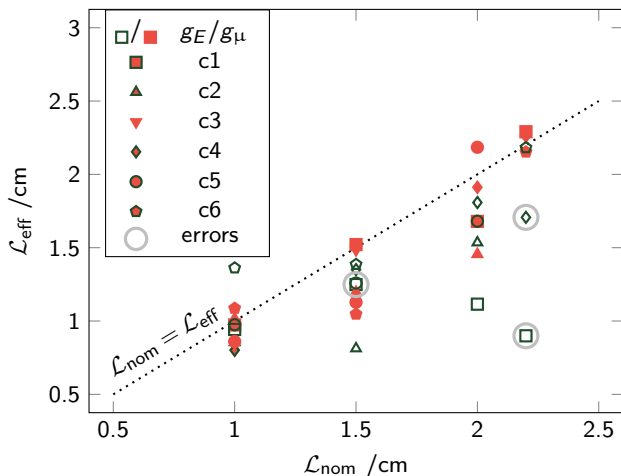


FIG. 4. Verification of the extruded volumes: equivalent sphere diameter $\mathcal{L}_{\text{eff}} = (6/\pi)V_{\text{exp}}$ from the numerically reconstructed droplet volumes, as a function of their nominal size \mathcal{L} . Full symbols correspond to droplets in microgravity experiments, open symbols to those under Earth gravity; symbol shapes indicate the various Carbopol concentrations as labeled. The dotted line is the expected $\mathcal{L}_{\text{eff}} = \mathcal{L}$.

the fluids, and the syringes were driven by precisely controlled linear motors. However, the tubing connecting the syringes and extrusion needles has finite stiffness, which can result in a quantity of extruded material that is lower than expected. There may also be fluid loss into the pre-wetting film. Both these sources of error are compatible with a systematic underestimation of \mathcal{L} .

B. Scaling laws

Jalaal, Stoeber, and Balmforth [11] derived scaling laws for the dependence of the final droplet radius on the dimensionless numbers \mathcal{B} and \mathcal{J} . These scaling laws arise from an asymptotic analysis of the thin-film equations, using the Bingham model as a constitutive equation for the stress tensor. One obtains for the final radius of the droplet

$$\frac{R}{\mathcal{L}} \simeq \begin{cases} \frac{1}{2} \left(\frac{25}{32} \right)^{1/5} \mathcal{B}^{1/5} \mathcal{J}^{-1/5}, & \mathcal{B} \gg 1, \\ \beta \cdot \mathcal{J}^{-1/7}, & \mathcal{B} \rightarrow 0, \end{cases} \quad (7)$$

with $\beta \approx 0.87$ (converting the results of Ref. [11] to our convention that introduces a factor of 2 in \mathcal{L} , as we define \mathcal{L} as the diameter of the equivalent sphere, not its radius). Accounting for conservation of fluid volume, in three dimensions, this implies

$$\frac{h}{\mathcal{L}} \sim \begin{cases} 4\alpha \left(\frac{32}{25} \right)^{2/5} \mathcal{B}^{-2/5} \mathcal{J}^{2/5}, & \mathcal{B} \gg 1, \\ \alpha \beta^{-2} \mathcal{J}^{2/7}, & \mathcal{B} \rightarrow 0. \end{cases} \quad (8)$$

with a prefactor α that depends on the droplet shape and is $\alpha = (3/2\pi)(\pi/6) = 1/4$ for droplets of ellipsoidal shape with a volume equal to a sphere of diameter \mathcal{L} .

These scaling laws are in principle free of fit parameters. However, they require knowledge of the surface tension in the case $\mathcal{B} \rightarrow 0$, entering through the definition of the plasto-capillary number \mathcal{J} . In the following we assume a fixed value of $\hat{\sigma} = 72 \text{ mN/m}$, assuming that the surface tension of the aqueous solutions is close enough to that of pure water. We will comment on this assumption in Sec. IV.

Figure 5 shows the experimentally measured heights and radii of the droplets in dependence of the non-dimensional number \mathcal{J} . Lines represent the scaling laws. For the case of the droplet radii, the analytically calculated prefactors have been used, thus there are no free fit parameters in this comparison. We observe that all data are compatible with the two predicted power laws, $R \sim \mathcal{J}^{-1/7}$ without gravitational acceleration, and $R \sim \mathcal{J}^{-1/5}$ for the ground experiments. The height data follow the respective power laws, however especially in the ground experiments, stronger deviations are seen, including also the simulation data of $\mathcal{L} = 1 \text{ cm}$. Note that the theoretical predictions for the height have to assume a certain droplet shape, so that potentially some deviations can be attributed to this. Specifically, we assume ellipsoidal shapes as discussed in conjunction with Eq. (8), $\alpha = 1/4$. Possible sources of error coming from the experiment include the fact that the droplets are extruded through a needle that remains fixed in the center of the droplet. Hence capillary rise of the fluid around the needle cannot be completely avoided. This influences both the droplet height and its determination in image analysis. However, this would likely lead to an over-estimation of the true height, whereas the deviations we observe in Fig. 5(c) are systematically towards lower values.

In the data from the microgravity experiments, we observe a systematic deviation most notably in the droplet radii: the experimentally determined values fall below the analytical prediction. This effect had also been seen in Ref. [11] where the limit $\mathcal{B} \rightarrow 0$ could only be realized by letting $\mathcal{L} \rightarrow 0$. Indeed, also in our microgravity experiments, deviations appear to be most pronounced for the smallest \mathcal{L} [blue triangles in Fig. 5(b)], while the $\mathcal{L} = 2.2 \text{ cm}$ data appears to be somewhat closer to the prediction (green circles). However, the quality of our data does not allow to conclude a systematic effect. In the simulations (open symbols) the predicted analytical law is quantitatively fulfilled for all \mathcal{L} ; this would attribute deviations for small \mathcal{L} in the experiment to the details of the extrusion mechanism and highlight the difficulty of analyzing small droplets.

Let us investigate the deviations in more detail. Figure 6 repeats the radii obtained from the microgravity experiments, but in the fully non-dimensionalized form suggested by Eq. (7), *i.e.*, R/\mathcal{L} as a function of \mathcal{J} . This confirms the data collapse predicted by the scaling law to within 20% and highlights the systematic overestimation of the radii by the theory.

In principle, a premature drying of the thin liquid film on the substrate on which the droplet is spreading, can contribute to a lesser spread than expected. However, we do not expect this to be a systematic effect. Incomplete extrusion as indicated by the fact that $\mathcal{L}_{\text{eff}} < \mathcal{L}$ in the image analysis, could explain a systematic deviation towards lower radii. We thus show in Fig. 6 a comparison of the data from the microgravity experiments

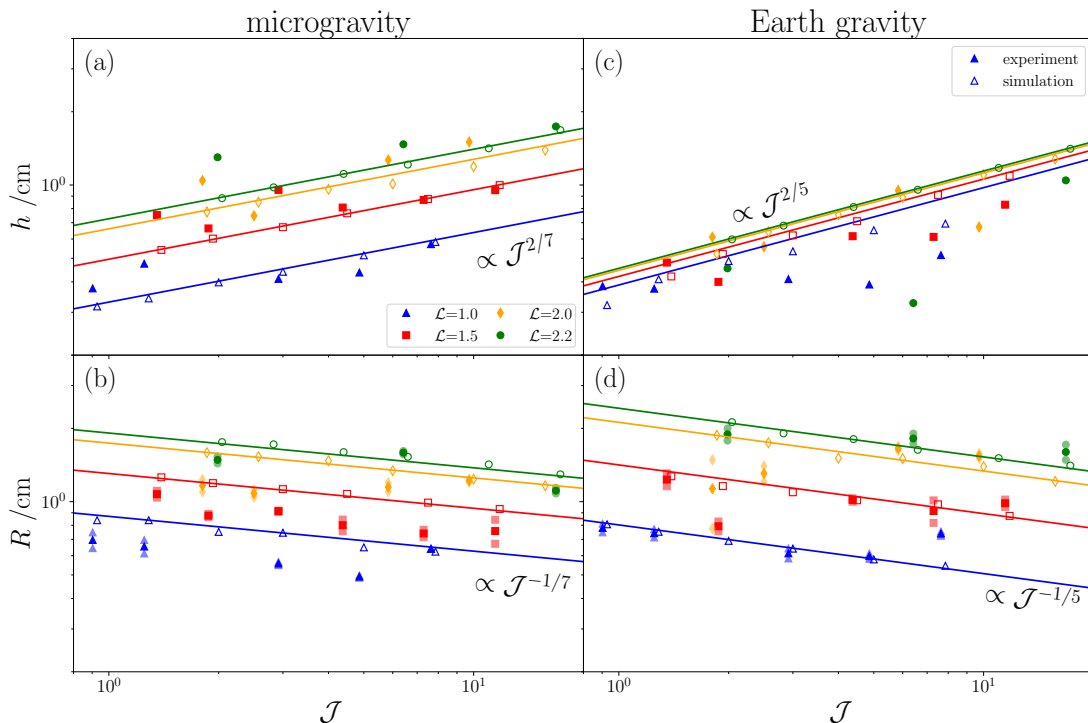


FIG. 5. Test of the scaling laws of Ref. [11] for final droplet sizes as a function of viscoplastic number \mathcal{J} , for different sizes \mathcal{L} . Filled symbols correspond to the experimental data ($\mathcal{L} = 1.0$ cm to 2.2 cm as labeled), open symbols to simulations for height (top row) and radius (bottom row); (a) and (b) refer to microgravity data, $\mathcal{B} \approx 0$, while (c) and (d) refer to data for $\mathcal{B} \gg 1$. Lines in all panels correspond to the expressions given in Eqs. (7) and (8); for the height values, hemi-spherical droplets were assumed in evaluating a global prefactor. In (b) and (d) light-filled symbols indicate separate estimates for the radii to indicate image-analysis error.

to the scaling prediction, where we also correct the nominal droplet sizes \mathcal{L} to the measured ones \mathcal{L}_{eff} (symbols with error bars). Note that this also shifts the dimensionless numbers to corrected ones, \mathcal{J}_{eff} and \mathcal{B}_{eff} .

From theoretical considerations of an elasto-viscoplastic model [12], one concludes that elastic effects that are not considered in the Bingham model behind Eq. (7) should suppress spreading. In the limit of weak elasticity in this model, the leading-order correction can be captured by a reduction of the prefactor of the visco-plastic power law. Such fits, introducing an *ad hoc* prefactor in Eq. (7), are shown in Fig. 6 for the data both using the nominal and the experimental determined value of the length scale. We observe that the deviation is on the order of 10% to 20%.

Let us note that attributing these deviations to finite elasticity is subtle: our simulations employ a model that also contains elasticity, but in the form of a visco-elastic liquid-material model, with a dynamical yield stress that emerges as the flow rate drops below the relaxation rate of the material. The asymptotic droplet shapes obtained from the model agree well with the prediction based on the Bingham model, except for systematic deviations in the $\mathcal{L} = 1$ case, that can be attributed to the finite h_{∞} ; for a more detailed explanation of the simulation analysis we refer to Sec. III C below. In contrast, in Ref. [12], an elasto-viscoplastic solid-material model with a static yield stress. For the model used in the simulations here, no in-depth theoretical analysis is available yet.

Also the gravity-based data collapses onto a master curve. According to Eq. (7), the normalized radii R/\mathcal{L} become a unique function of $(\mathcal{J}/\mathcal{B})$ for all droplet sizes. This is verified with our data in Fig. 7 for which we observe the predicted collapse to within experimental errors. The possible correction to the nominal \mathcal{L} coming from our image analysis plays a sub-leading role here, as both data sets, R/\mathcal{L} as a function of \mathcal{J}/\mathcal{B} (filled symbols in Fig. 7), and $R/\mathcal{L}_{\text{eff}}$ as a function of $\mathcal{J}_{\text{eff}}/\mathcal{B}_{\text{eff}}$ (symbols with error bars), do not show any systematic deviation from the prediction.

The shape of the droplets, for fixed volume, depends on their yield stress and on the presence or absence of gravity. We have extracted the aspect ratio of the droplets, $\Phi = h/R$, from the experiments. A value of $\Phi = 1$ indicates a hemi-spherical droplet, while for $\Phi < 1$, droplet shapes are oblate, and $\Phi > 1$ indicates prolate droplets.

Combining the scaling laws, Eqs. (7) and (8), one easily obtains analytical predictions for the aspect ratio, $\Phi \sim \mathcal{J}^{3/7}$ for the microgravity case $\mathcal{B} \rightarrow 0$, and $\Phi \sim \mathcal{J}/\mathcal{B}^{3/5}$ in the presence of gravity, $\mathcal{B} \gg 1$. We show these predictions together with the aspect ratios from our experiments in Fig. 8. For the analytical prediction, we assumed ellipsoidal droplet shapes (setting $\alpha = 1/4$) but used no fitting parameter otherwise. Both these asymptotes imply $\Phi \gg 1$ for large enough \mathcal{J} . For the microgravity conditions, our experimental values span the regime of both $\Phi < 1$ and $\Phi > 1$. In the ground-based experiments, we observe $\Phi < 1$ for all droplets, *i.e.*, they are

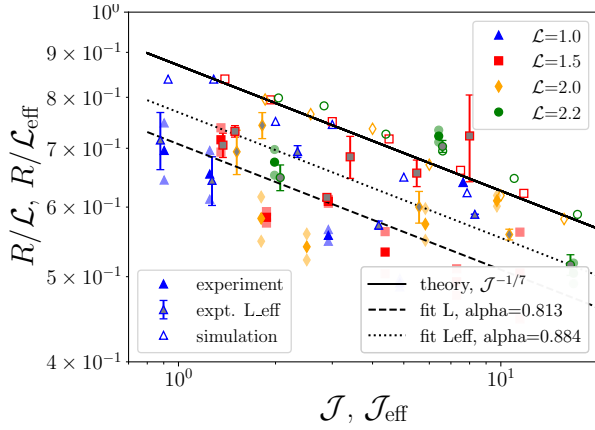


FIG. 6. Scaling plot for the droplet radii in the regime $\mathcal{B} \rightarrow 0$: normalized radii R/\mathcal{L} are shown as a function of the plasto-capillary number \mathcal{J} . Filled and open symbols correspond data from microgravity experiments and simulations, respectively. A solid line represents the theoretical result, Eq. (7). Symbols with error bars are experimental values corrected for the extruded volume (see text for details). A dashed (dotted) line represents the theory with an ad-hoc adjusted prefactor as noted in the legend, obtained from a fit of the experimental data without (with) this correction.

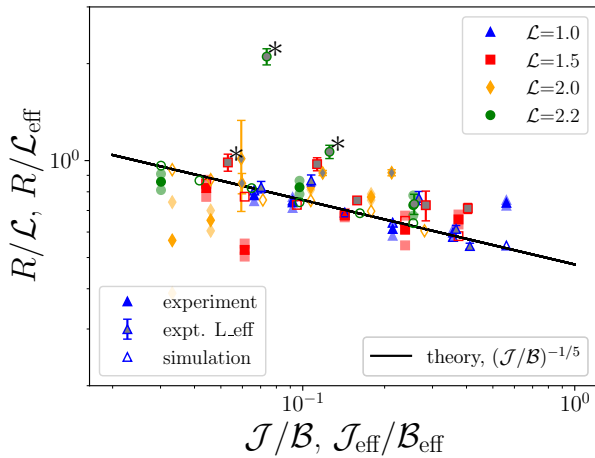


FIG. 7. Scaling plot for the droplet radii in the regime $\mathcal{B} \neq 0$: normalized radii R/\mathcal{L} as a function of \mathcal{J}/\mathcal{B} . Filled and open symbols correspond to data from experiment and simulations, respectively. A solid line represents the theoretical result, Eq. (7). Symbols with error bars are experimental values corrected for \mathcal{L}_{eff} . Stars next to symbols indicate outliers as assessed by the quality of the image analysis.

all oblate even for those combinations of τ_0 and \mathcal{L} where the scaling laws suggest to reach the regime of prolate droplets also under gravity.

Note that the numbers \mathcal{J} and \mathcal{J}/\mathcal{B} are proportional to the yield stress τ_0 . Thus from the droplets' aspect ratio shown in Fig. 8, we confirm previous results by German and Bertola [53]: a higher yield stress always increases droplets' aspect ratio. This correlation can be attributed to the fact that a higher yield stress results in a larger immobile regions inside the droplet, which can be lifted up while remaining immobile during deposition. The final droplet shape hence becomes

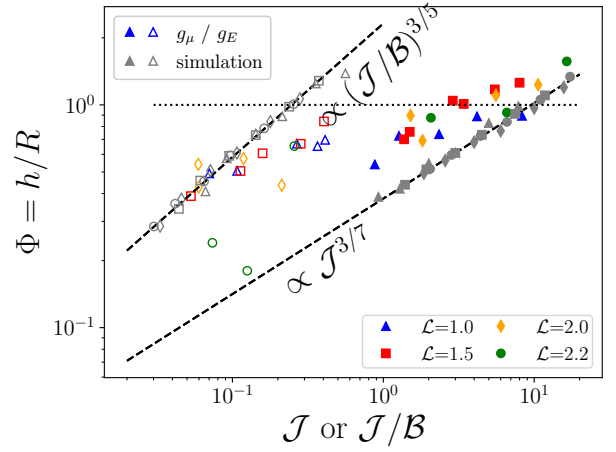


FIG. 8. Geometrical aspect ratio, $\Phi = h/R$, as a function of the plasto-capillary number (for the case in microgravity) and as a function of \mathcal{J}/\mathcal{B} (for the case with gravity). Black dashed lines correspond to the theoretical predictions. Full symbols correspond to data from microgravity experiments, open symbols to those in Earth gravity. Grey symbols represent the simulation results.

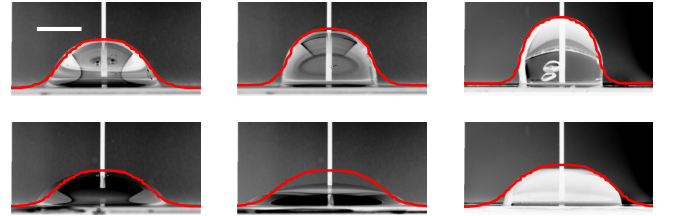


FIG. 9. Illustration of droplet shapes for droplets with size $\mathcal{L} = 2.2$ cm: The top row shows images from microgravity experiments; the bottom row the corresponding results on ground. Different Carbopol concentrations are shown, with increasing yield stress from left to right (concentrations c_1 , c_4 , and c_6). The white scale bar in the top left panel represents 1 cm. Red lines indicate results from simulations with a shear-thinning Maxwell fluid, using various shear moduli G_∞ to match the experimental yield-stress values. The large deviation in the center bottom panel is attributed to an experimental problem during droplet extrusion.

elongated upwards.

C. Comparison to Simulations

Figure 9 shows exemplary cases of droplets for $\mathcal{L} = 2.2$ cm and different yield stresses (Carbopol concentrations). In the microgravity experiment one clearly sees the evolution towards more prolate droplets with increasing yield stress.

Also shown in Fig. 9 are simulation results for asymptotic droplet shapes (red lines). They confirm that our viscoelastic shear-thinning fluid model is able to capture the specific droplet shapes well. Deviations are seen towards to bottom. But note that the simulations use a rather high background-fluid layer for numerical stability, which results in droplet shapes that are much more “rounded” than the ones in experiment towards

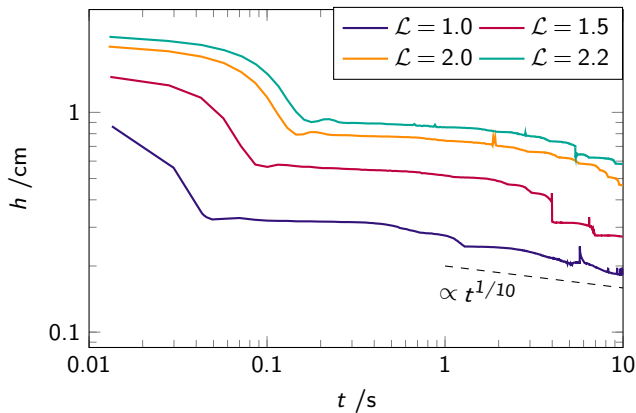


FIG. 10. Height evolution as a function of time in the simulations; shown for a yield stress of $\tau_0 = 6.5$ Pa (c1), and different droplet sizes \mathcal{L} as labeled.

the bottom, missing a clearly defined contact line. In fact, in the experiment the apparent contact angles increase with increasing yield stress [34], and they increase in the microgravity experiment compared to the one in Earth gravity. For the largest yield stress shown in Fig. 9, the apparent contact angle exceeds 90° ; an effect not observed in the simulation.

To illustrate how the asymptotic droplet shapes are extracted from the simulation, we show in Fig. 10 exemplary results for the evolution of the droplet height in the simulation. Results are shown for fixed yield stress without gravity, and different \mathcal{L} . Typically for a visco-elastic fluid model, the height shows an initial decrease at short times, driven by surface tension adjusting the shape of the droplet from the arbitrarily chosen initial configuration. For large droplets, this evolution hints at some oscillations (around $t = 0.2$ s in the figure for $\mathcal{L} = 2.0$ and $\mathcal{L} = 2.2$), indicative of elastic restoring forces. After this initial decay, a plateau is observed in the height-*versus*-time plot. Recall that our model always allows flow on time scales $t \gg \tau$, but acts like a yield-stress fluid for $t \ll \tau$. We thus extract the asymptotic droplet shape that represents the balance of the yield stress with the other forces (surface tension and gravity) in the plateau regime that is (within the limits that we checked) independent of the precise initial conditions and not yet affected by the ultimate liquid-like flow of the model.

The simulation allows to address the role of the fluid rheology in determining the droplet shapes. Recall that the scaling laws were obtained for a model viscoplastic fluid, where a yield stress is incorporated in an ad-hoc manner. The good agreement with our simulations of a refined model of a visco-elastic shear-thinning fluid is encouraging: in the asymptotic long-time regime that we analyze, only the value of the (dynamic) yield stress τ_0 enters.

On purely dimensional grounds, also elastic effects might be considered, *i.e.*, the balance of elastic restoring forces (quantified by the shear modulus G_∞ of the viscoelastic fluid) compared to surface-tension forces. However, the droplet shapes observed in experiment are clearly determined by the dynamic yield stress. To assert this, we compare in Fig. 11 droplet shapes obtained from the simulation with and without shear

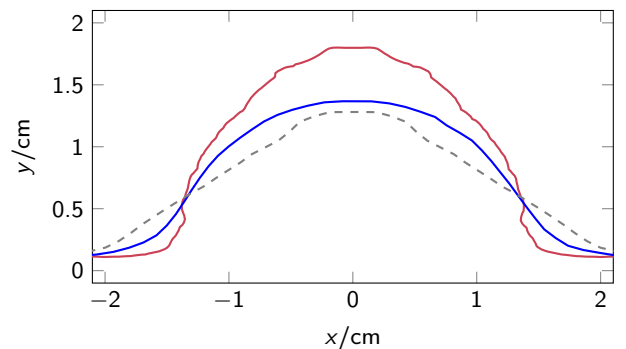


FIG. 11. Shape of a droplet for $G_\infty = 32.5$ Pa and $R = 0.02$ m. Red: simulation results for the case without shear-thinning, blue: simulation results for the case with shear-thinning ($\gamma_c = 1/5$). The case without shear thinning, but effective reduced shear modulus $G_\infty^{\text{eff}} = G_\infty \gamma_c$ is shown as a dashed line for comparison.

thinning. We observe that the purely viscoelastic droplet (red line in Fig. 11) remains taller and less spread compared to the one with shear thinning: shear thinning initially aids the flow of the material in response to the surface tension forces. The forces opposing the complete spread of the droplet are then given by the yield stress, $\tau_0 = G_\infty \gamma_c$, and these are not equivalent to a simply reduced elastic force G_∞^{eff} : as the comparison with the model without shear thinning, but $G_\infty^{\text{eff}} = G_\infty \gamma_c$ shows (dashed line), the droplet shapes are not identical with and without shear thinning.

IV. CONCLUSION

We studied the spreading of droplets of Carbopol suspensions, a model yield stress fluid, both with and without gravitational acceleration. The droplets spread on a pre-wetted thin film, and eventually attain a finite shape, due to a balance between surface tension, their yield stress, and hydrostatic pressure in the presence of gravity. Conducting microgravity experiments at the ZARM drop tower, we were able to separate the limit $\mathcal{B} \rightarrow 0$ from the limit $\mathcal{J} \rightarrow 0$ by decoupling \mathcal{B} from the droplet size, \mathcal{L} . We could hence verify scaling laws by Jalaal, Stoeber, and Balmforth [11] for both the gravity-dominated case (characterized by finite Bond number, $\mathcal{B} \gg 1$) and the surface-tension dominated case ($\mathcal{B} \rightarrow 0$, at finite plastocapillary number \mathcal{J}). We complemented our experiments by simulations using a model including a dynamical yield stress together with visco-elasticity, and found that the simulations obey the scaling predictions very well.

The scaling laws predict a power-law dependence of the final droplet size on the plastocapillary number, \mathcal{J} . For the experimental droplet radii we find good agreement with the predictions, while the droplet heights show somewhat larger deviations, especially in the gravity-dominated case.

Using a standard viscoplastic constitutive equation, *viz.* the Bingham model, Jalaal, Stoeber, and Balmforth also derived the numerical values of the prefactors in the scaling laws. Our experimental results confirm these prefactors, but show that

in order to observe them, the limit $\mathcal{L} \rightarrow 0$ should be avoided if $\mathcal{B} \rightarrow 0$. Systematic deviations could point to finite elasticity effects as discussed more recently by França, Jalaal, and Oishi [12]. There, an extension of the Bingham model to include both a static yield stress and solid elasticity was studied, and corrections to the scaling laws coming from finite Ohnesorg and Deborah number would be compatible with our experimental data. Note however that our simulations show good agreement with the theoretical predictions based on the Bingham model, even though our simulation model includes visco-elastic effects. This is a subtle point: our model is ultimately a liquid-like model, with a regularized *dynamical* yield stress. The model of França, Jalaal, and Oishi in contrast has a *static* yield stress and included elasticity in a solid-like model. The connection between these different constitutive modelling approaches will have to be investigated further.

A potential cause of deviations from the scaling laws could be hidden in the role of the surface tension. In our analysis, we have assumed all our Carbopol solutions to have the same surface tension as water, irrespective of their yield stress. This is in line with recent experiments [54], and the interpretation that Carbopol as a non-surfactant polymer should not drastically change the surface tension of the solvent. Note however that the determination of surface tension in the presence of a yield stress is intricate [55, 56], as the YSF approaches solid-like behavior and one in principle needs to distinguish surface tension and surface energy.

Making use of the scaling laws for the case $\mathcal{B} = 0$ one could in principle determine the surface tension from a measurement of the droplet radii or heights,

$$\hat{\sigma} = (R/\beta)^7 \mathcal{L}^{-6} \tau_0 \quad (9)$$

respectively

$$\hat{\sigma} = (1/2\beta\sqrt{h})^7 \mathcal{L}^{9/2} \tau_0. \quad (10)$$

In principle, data from microgravity experiments would be uniquely suited to determine $\hat{\sigma}$ this way, because the expected variation with \mathcal{L} can be tested for fixed τ_0 and not leaving the required $\mathcal{B} \rightarrow 0$ regime. However, the high powers of R and h entering the equations cause large uncertainties. For our data, the obtained values of $\hat{\sigma}$ are still compatible with the value of the pure solvent.

DATA MANAGEMENT

The data associated to this study is available on Zenodo repositories 15806543 and 15806731 [36].

ACKNOWLEDGMENTS

We warmly acknowledge engineering support from the Technical Center from the University of Amsterdam, in particular Kasper van Nieuwland, Clint Ederveen Janssen Tjeerd G.L.C. Weijers and Daan Giesen, as well as the entire ZARM support team.

The authors gratefully acknowledge the scientific support and HPC resources provided by the German Aerospace Center (DLR). The HPC system CARO is partially funded by “Ministry of Science and Culture of Lower Saxony” and “Federal Ministry for Economic Affairs and Climate Action”.

O. D’A. acknowledges financial support from the European Low Gravity Research Association (ELGRA), who initially supported this project through the 2021 ELGRA Research Prize, and French National Centre for Space Studies (CNES) under the CNES fellowship 24-357.

- ¹N. J. Balmforth, I. A. Frigaard, and G. Ovarlez, “Yielding to stress: Recent developments in viscoplastic fluid mechanics,” *Annu. Rev. Fluid Mech.* **46**, 121–146 (2014).
- ²D. Bonn, M. M. Denn, L. Berthier, T. Divoux, and S. Manneville, “Yield stress materials in soft condensed matter,” *Reviews of Modern Physics* **89**, 035005 (2017).
- ³P. Coussot, *Rheophysics: Matter in all its States* (Springer, New York, 2014).
- ⁴J. K. Placone and A. J. Engler, “Recent advances in extrusion-based 3d printing for biomedical applications,” *Advanced healthcare materials* **7**, 1701161 (2018).
- ⁵S. Kyle, Z. M. Jessop, A. Al-Sabah, and I. S. Whitaker, “‘printability’ of candidate biomaterials for extrusion based 3d printing: state-of-the-art,” *Advanced healthcare materials* **6**, 1700264 (2017).
- ⁶Z. Jiang, B. Diggle, M. L. Tan, J. Viktorova, C. W. Bennett, and L. A. Connal, “Extrusion 3d printing of polymeric materials with advanced properties,” *Advanced Science* **7**, 2001379 (2020).
- ⁷R. A. Buswell, W. L. De Silva, S. Z. Jones, and J. Dirrenberger, “3d printing using concrete extrusion: A roadmap for research,” *Cement and concrete research* **112**, 37–49 (2018).
- ⁸J. van der Kolk, D. Tieman, and M. Jalaal, “Viscoplastic lines: printing a single filament of yield stress material on a surface,” *Journal of Fluid Mechanics* **958**, A34 (2023).
- ⁹S. L. Cormier, J. D. McGraw, T. Salez, E. Raphaël, and K. Dalnoki-Veress, “Beyond tanner’s law: Crossover between spreading regimes of a viscous droplet<? format=> on an identical film,” *Physical review letters* **109**, 154501 (2012).
- ¹⁰M. S. Agrawal, H. S. Gaikwad, P. K. Mondal, and G. Biswas, “Analysis and experiments on the spreading dynamics of a viscoelastic drop,” *Applied Mathematical Modelling* **75**, 201–209 (2019).
- ¹¹M. Jalaal, B. Stoeber, and N. J. Balmforth, “Spreading of viscoplastic droplets,” *Journal of Fluid Mechanics* **914**, A21 (2021).
- ¹²H. L. França, M. Jalaal, and C. M. Oishi, “Elasto-viscoplastic spreading: From plastocapillarity to elastocapillarity,” *Physical Review Research* **6**, 013226 (2024).
- ¹³N. Paxton, W. Smolan, T. Böck, F. Melchels, J. Groll, and T. Jungst, “Proposal to assess printability of bioinks for extrusion-based bioprinting and evaluation of rheological properties governing bioprintability,” *Biofabrication* **9**, 044107 (2017).
- ¹⁴J. M. Townsend, E. C. Beck, S. H. Gehrke, C. J. Berkland, and M. S. Detamore, “Flow behavior prior to crosslinking: The need for precursor rheology for placement of hydrogels in medical applications and for 3d bioprinting,” *Prog. Polym. Sci.* **91**, 126–140 (2019).
- ¹⁵M. Milazzo, V. Fitzpatrick, C. E. Owens, I. M. Carraretto, G. H. McKinley, D. L. Kaplan, and M. J. Buehler, “3d printability of silk/hydroxyapatite composites for microprosthetic applications,” *ACS Biomater. Sci. Eng.* **9**, 1285–1295 (2023).
- ¹⁶A. V. Ombergen, F. Chalupa-Gantner, P. Chansoria, B. M. Colosimo, M. Costantini, M. Domingos, A. Dufour, C. De Maria, J. Groll, T. Jungst, R. Levato, J. Malda, A. Margarita, C. Marquette, A. Ovsianikov, E. Petiot, S. Read, L. Surdo, W. Swieszkowski, G. Vozzi, J. Windisch, M. Zenobi-Wong, and M. Gelinsky, “3d bioprinting in microgravity: Opportunities, challenges, and possible applications in space,” *Adv. Healthcare Mater.* **12**, 2300443 (2023).
- ¹⁷A. Passerone, “Twenty years of surface tension measurements in space,” *Micrograv. Sci. Technol.* **23**, 101–111 (2011).
- ¹⁸A. Ababneh, A. Amirfazli, and J. A. W. Elliott, “Effect of gravity on the macroscopic advancing contact angle of sessile drops,” *Can. J. Chem. Engin.* **84**, 39–43 (2006).

- ¹⁹A. Diana, M. Castillo, D. Brutin, and T. Steinberg, “Sessile drop wettability in normal and reduced gravity,” *Micrograv. Sci. Technol.* **24**, 195–202 (2012).
- ²⁰A. Baldygin, A. Ahmed, R. Bailly, M. F. Ismail, M. Khan, N. Rodrigues, A.-R. Salehi, M. Ramesh, S. Bhattacharya, T. Willers, *et al.*, “Effect of gravity on the spreading of a droplet deposited by liquid needle deposition technique,” *npj Microgravity* **9**, 49 (2023).
- ²¹B. Mielniczuk, O. Millet, G. Gagneux, and M. S. El Youssoufi, “Characterisation of pendular capillary bridges derived from experimental data using inverse problem method,” *Granular Matter* **20**, 14 (2018).
- ²²J. McCraney, V. Kern, J. B. Bostwick, S. Daniel, and P. H. Steen, “Oscillations of drops with mobile contact lines on the international space station: Elucidation of terrestrial inertial droplet spreading,” *Phys. Rev. Lett.* **129**, 084501 (2022).
- ²³J. McCraney, J. Ludwicki, J. Bostwick, S. Daniel, and P. Steen, “Coalescence-induced droplet spreading: Experiments aboard the international space station,” *Physics of Fluids* **34** (2022).
- ²⁴S. I. Tamim and J. B. Bostwick, “Oscillations of a soft viscoelastic drop,” *npj Microgravity* **7**, 42 (2021).
- ²⁵A. Saïdi, C. Martin, and A. Magnin, “Influence of yield stress on the fluid droplet impact control,” *Journal of Non-Newtonian Fluid Mechanics* **165**, 596–606 (2010).
- ²⁶B. Gorin, G. Di Mauro, D. Bonn, and H. Kellay, “Universal aspects of droplet spreading dynamics in newtonian and non-newtonian fluids,” *Langmuir* **38**, 2608–2613 (2022).
- ²⁷M. H. Biroun, L. Haworth, H. Abdolnezhad, A. Khosravi, P. Agrawal, G. McHale, H. Torun, C. Semperebon, M. Jabbari, and Y.-Q. Fu, “Impact dynamics of non-newtonian droplets on superhydrophobic surfaces,” *Langmuir* **39**, 5793–5802 (2023).
- ²⁸A. Mobaseri, S. Kumar, and X. Cheng, “Maximum spreading of impacting shear-thinning and shear-thickening drops,” *Proceedings of the National Academy of Sciences* **122**, e2500163122 (2025).
- ²⁹S. Jung, S. D. Hoath, and I. M. Hutchings, “The role of viscoelasticity in drop impact and spreading for inkjet printing of polymer solution on a wettable surface,” *Microfluidics and nanofluidics* **14**, 163–169 (2013).
- ³⁰V. Bertola, “An experimental study of bouncing leidenfrost drops: comparison between newtonian and viscoelastic liquids,” *International journal of heat and mass transfer* **52**, 1786–1793 (2009).
- ³¹H. Dittus, “Drop tower ‘bremen’: a weightlessness laboratory on earth,” *Endeavour* **15**, 72–78 (1991).
- ³²P. Von Kampen, U. Kaczmarczik, and H. J. Rath, “The new drop tower catapult system,” *Acta Astronautica* **59**, 278–283 (2006).
- ³³H. Dittus and A. Schomisch, “Vacuum systems for microgravity experiments,” *Vacuum* **41**, 2135–2137 (1990).
- ³⁴O. D’Angelo, F. Kuthe, K. van Nieuwland, C. Ederveen Janssen, T. Voigtmann, and M. Jalaal, “Spreading of droplets under various gravitational accelerations,” *Review of Scientific Instruments* **93** (2022), 10.1063/5.0105624, 115103.
- ³⁵M. Jalaal, N. J. Balmforth, and B. Stoeber, “Slip of spreading viscoplastic droplets,” *Langmuir* **31**, 12071–12075 (2015).
- ³⁶O. D’Angelo, L. Heitmeier, and T. Voigtmann, “VIP-DROP experimental data,” (2025), DOI:10.5281/zenodo.15806543; “VIP-DROP Experimental Data for PIV,” (2025).
- ³⁷B. Barry and M. Meyer, “The rheological properties of carbopol gels i. continuous shear and creep properties of carbopol gels,” *International journal of pharmaceuticals* **2**, 1–25 (1979).
- ³⁸S. Curran, R. Hayes, A. Afacan, M. Williams, and P. A. Tanguy, “Properties of carbopol solutions as models for yield-stress fluids,” *Journal of food science* **67**, 176–180 (2002).
- ³⁹E. Di Giuseppe, F. Corbi, F. Funiciello, A. Massmeyer, T. Santimano, M. Rosenau, and A. Davaille, “Characterization of carbopol® hydrogel rheology for experimental tectonics and geodynamics,” *Tectonophysics* **642**, 29–45 (2015).
- ⁴⁰I. Frigaard, “Simple yield stress fluids,” *Current Opinion in Colloid & Interface Science* **43**, 80–93 (2019).
- ⁴¹M. Jalaal, D. Kemper, and D. Lohse, “Viscoplastic water entry,” *Journal of Fluid Mechanics* **864**, 596–613 (2019).
- ⁴²G. Martouzet, L. Jørgensen, Y. Pelet, A.-L. Biance, and C. Barentin, “Dynamic arrest during the spreading of a yield stress fluid drop,” *Phys. Rev. Fluids* **6**, 044006 (2021).
- ⁴³*Basilisk*.
- ⁴⁴S. Popinet, “An accurate adaptive solver for surface-tension-driven interfacial flows,” *Journal of Computational Physics* **228**, 5838–5866 (2009).
- ⁴⁵A. Prosperetti, *Computational Methods for Multiphase Flow* (Cambridge university press, 2009).
- ⁴⁶G. Tryggvason, R. Scardovelli, and S. Zaleski, *Direct numerical simulations of gas-liquid multiphase flows* (Cambridge university press, 2011).
- ⁴⁷A. G. Balasubramanian, V. Sanjay, M. Jalaal, R. Vinuesa, and O. Tammisola, “Bursting bubble in an elastoviscoplastic medium,” *Journal of Fluid Mechanics* **1001**, A9 (2024).
- ⁴⁸V. Sanjay, D. Lohse, and M. Jalaal, “Bursting bubble in a viscoplastic medium,” *Journal of fluid mechanics* **922**, A2 (2021).
- ⁴⁹B. Zhang, V. Sanjay, S. Shi, Y. Zhao, C. Lv, X.-Q. Feng, and D. Lohse, “Impact forces of water drops falling on superhydrophobic surfaces,” *Physical review letters* **129**, 104501 (2022).
- ⁵⁰M. Fuchs and M. E. Cates, “Schematic models for dynamic yielding of sheared colloidal glasses,” in *Non-equilibrium Behaviour of Colloidal Dispersions*, Vol. 123 (2003) pp. 267–286.
- ⁵¹S. Papenkort and T. Voigtmann, “Lattice boltzmann simulations of a viscoelastic shear-thinning fluid,” *J. Chem. Phys.* **143**, 044512 (2015).
- ⁵²J. G. Oldroyd, “On the formulation of rheological equations of state,” *Proceedings of the Royal Society of London. Series A. Mathematical and Physical Sciences* **200**, 523–541 (1950).
- ⁵³G. German and V. Bertola, “Impact of shear-thinning and yield-stress drops on solid substrates,” *Journal of Physics: Condensed Matter* **21**, 375111 (2009).
- ⁵⁴H. Mohammadigoushki and K. Shoele, “Cavitation rheology of model yield stress fluids based on carbopol,” *Langmuir* **39**, 7672–7683 (2023).
- ⁵⁵J. Boujlel and P. Coussot, “Measuring the surface tension of yield stress fluids,” *Soft Matter* **9**, 5898–5908 (2013).
- ⁵⁶L. Jørgensen, M. Le Merrer, H. Delanoë-Ayari, and C. Barentin, “Yield stress and elasticity influence on surface tension measurements,” *Soft Matter* **11**, 5111–5121 (2015).

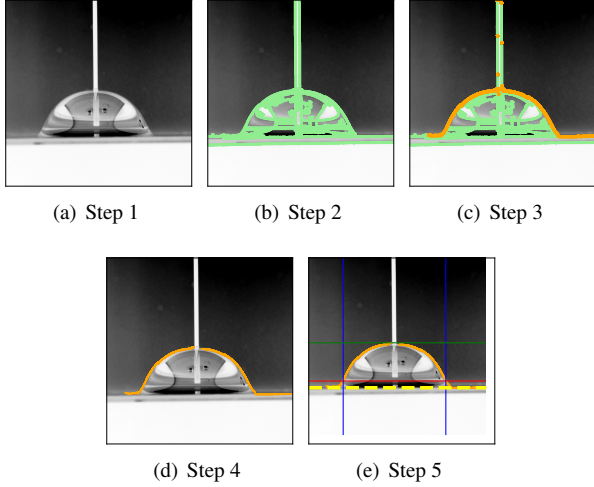


FIG. 12. Steps in the image analysis. See text for a deeper description.

APPENDIX

Appendix A: Data analysis of the experimental data

We briefly summarize our image analysis procedure to obtain the droplet shapes. We analyze the images from the experiment in 5 different steps, as sketched in Figure 12.

From the video recording of the experiment, we extract the raw image of the droplet in the late stage of the experiment (just before impact in the microgravity case), as in Fig. 12(a). We first identify all edges in the images with a canny-edge filter (standard OpenCV implementation in python, `cv2.Canny`, using thresholds of 48 % and 52% of the maximal image pixel. This step is illustrated in Fig. 12(b). To keep only the outer shape of the droplet, all edges detected inside the droplet (typically from small air inclusions or reflections) are removed. This is done by deleting, for every x -values, every y -value except the highest value. The outer shape of the droplet thus found is marked yellow in Fig. 12(c). As the deposition needle, which is part of the experimental images, should not be part of our analysis, we then delete all values which have an x -value in the range of that of the needle. The resulting image can be seen in Fig. 12(d).

Finally, we perform the analysis of the extracted droplet

shape. The bottom of the droplet (thin film of pre-wetting fluid), placed at height h_0 , is found by taking the minimum value of the y -values of the droplet shape. This is marked by the dashed yellow line in Fig. 12(e). The height of the droplet, h , can be extracted by taking the maximum value of the y -values of the droplet's shape. The height of the droplet is drawn as a green line in Fig. 12(e). The radius is determined by defining a new height, h_{radius} , given by $h_0 + (h - h_0) \cdot 0.1$, which is drawn in red in Fig. 12(e). This rise of 10% of the droplet's height from its bottom allows us to capture the droplets' radii without the wetting angle. We identify the x -values at which the shape of the droplet crosses this point to capture the droplet's extremities (blue lines in Fig. 12(e)).

The center of the image is defined by the position of the needle. To convert the values of the heights and radii obtained in image processing, before each experiment calibration images with a 2 mm grid were taken; the resolution of the setup is typically 15 px mm^{-1} .

We verified the circularity of the droplets by pictures taken from below the glass substrate (example in Figure 13(a)).

Another concern in the volume reconstruction by image analysis is the fact that light reflections sometimes affect the detection of the droplet's contour. One such example is given in Figure 13(b): on the right side of the image, the image analysis algorithm picks up a light reflection instead of the true droplet's shape. In such case, we used the well reconstructed half of the droplet (left half here) and determined its volume by mirroring it.

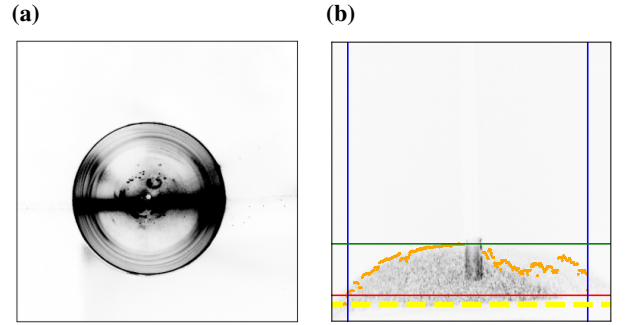


FIG. 13. Left: Image from the bottom from the droplet of concentration c_4 and $\mathcal{L} = 2.2$. Right: Exemplary image, where the shape detection did not work perfectly.